https://doi.org/10.5194/egusphere-2026-6804
Preprint. Discussion started: 12 November 2026
© Author(s) 2026. CC BY 4.0 License.

Single-scattering albedo drives Saharan dust forcing uncertainty and the simulated West African monsoon response in CMIP6 models

Wooseok Kang[1], Myong-In Lee[1,*], Kyu-Myong Kim[2], Kyung-On Boo[3], Pil-Hun Chang[3], and Hyomee Lee[3]

[1]Department of Civil, Urban, Earth and Environmental Engineering, Ulsan National Institute of Science and Technology, Ulsan, Republic of Korea

[2]NASA Goddard Space Flight Center, MD, United States

[3]Climate Change Research Team, National Institute of Meteorological Sciences, Jeju, Republic of Korea

*Correspondence to: Myong-In Lee (milee@unist.ac.kr)

Department of Civil, Urban, Earth and Environmental Engineering, Ulsan National Institute of Science and Technology, Ulsan, 44919, Republic of Korea

https://doi.org/10.5194/egusphere-2026-6804
Preprint. Discussion started: 12 November 2026
© Author(s) 2026. CC BY 4.0 License.



Abstract

Mineral dust affects the West African energy balance and monsoon circulation, yet climate models differ widely in the dust optical properties that set the balance between scattering and absorption. As a result, models disagree even on whether dust produces net shortwave (SW) warming or cooling over North Africa. Here we show that Saharan single-scattering albedo (SSA), an observable intensive optical property, accounts for much of the inter-model spread in the shortwave dust forcing response across climate models. The Saharan SW effective radiative forcing due to aerosol–radiation interactions ($\mathbf{ERF}_{\mathbf{ari}}^{\mathbf{SW}}$) decreases systematically with increasing SSA, shifting from near-zero or positive values in lower-SSA, more absorbing models to negative values in higher-SSA, more scattering models. Applying an Aerosol Robotic Network (AERONET)-based observational constraint on SSA, 0.9543 ± 0.0060, gives a constrained Saharan $\mathbf{ERF}_{\mathbf{ari}}^{\mathbf{SW}}$ centered near zero at −0.66 W m^{-2}, with a 95 % interval of −3.87 to +2.53 W m^{-2}.

Grouping the models by SSA reveals two contrasting monsoon responses to the same dust-emission perturbation. Low-SSA models show stronger atmospheric heating over the Sahara, a deeper heat low, enhanced monsoon inflow, and increased Sahel rainfall, whereas High-SSA models show a weaker or opposite response and reduced rainfall. The associated cloud-radiative response forms a Sahel–tropical North Atlantic dipole. Propagating the SSA-based constraint on the $\mathbf{ERF}_{\mathbf{ari}}^{\mathbf{SW}}$ through the relationship between Saharan $\mathbf{ERF}_{\mathbf{ari}}^{\mathbf{SW}}$ and Sahel cloud-radiative response reduces its inter-model variance by about one third. Thus, an observable dust optical property constrains a significant part of the downstream monsoon and cloud-response uncertainty.

https://doi.org/10.5194/egusphere-2026-6804
Preprint. Discussion started: 12 November 2026
© Author(s) 2026. CC BY 4.0 License.

1 Introduction

Mineral dust is the most abundant aerosol species in the atmosphere by mass (Kok et al., 2021), yet even the sign of the radiative forcing remains uncertain. The most recent assessment places the dust radiative effect at −0.2 W m^{-2}, with a 90 % confidence interval of −0.7 to +0.4 W m^{-2} (Kok et al., 2023), an interval that allows either net cooling or net warming. Multi-model estimates from Coupled Model Intercomparison Project Phase 6 (CMIP6) Earth system models (ESMs) likewise span both signs (Thornhill et al., 2021; Haugvaldstad et al., 2025). This uncertainty is especially important because atmospheric dust loading has changed over time. Observations indicate increases in dust amount in several regions since the beginning of the industrial era (Hooper and Marx, 2018; Mulitza et al., 2010), and one reconstruction estimates a global rise of roughly 55 ± 30 % (Kok et al., 2023). An aerosol burden that has increased, combined with a forcing whose sign remains uncertain, therefore complicates the interpretation of the historical forcing record and the attribution of warming to individual forcing agents. Dust perturbs the top-of-atmosphere (TOA) energy balance mainly through aerosol–radiation interactions in the shortwave (SW) and longwave (LW) radiation, with additional pathways through cloud condensation (Karydis et al., 2017) and ice nucleation (Storelvmo, 2017; Froyd et al., 2022), heterogeneous chemistry (Bauer et al., 2007), and surface albedo changes after deposition (Shi et al., 2021; Kok et al., 2023). Dust forcing can also affect climate beyond the TOA energy balance. By heating the atmospheric column while the surface temperature remains fixed, absorbing dust may increase static stability and alter circulation and precipitation (Miller et al., 2004). These diverse pathways, combined with weak observational constraints on dust optical properties, make the dust forcing one of the most uncertain among all forcing agents.

Among these pathways, the interaction of dust with SW radiation is the most firmly established in ESMs, and its dominant source of uncertainty is comparatively well understood. It is generally represented through the complex refractive index (CRI) of dust, which sets the balance between scattering and absorption and depends on the mineralogical composition of the particles (Di Biagio et al., 2019). Many ESMs, however, still rely on refractive indices derived from optical databases assembled in the early 2000s such as OPAC (Hess et al., 1998), which have been shown to overestimate SW absorption by dust (Adebiyi et al., 2023; Di Biagio et al., 2019). Replacing these older optical data with observationally constrained values substantially increases the modeled SW cooling (Obiso et al., 2024; Li et al., 2024). Because such updates have not been applied consistently across models, the inter-model spread in dust absorption has persisted across more than a decade of model intercomparison (Gliß et al., 2021; Huneeus et al., 2011). Although the dust forcing uncertainty also arises from other sources, including the particle size distribution and LW radiative effects (Dufresne et al., 2002; Kok et al., 2017), and each of these

https://doi.org/10.5194/egusphere-2026-6804
Preprint. Discussion started: 12 November 2026
© Author(s) 2026. CC BY 4.0 License.

sources requires its own observational constraint, here we narrow our focus to single scattering albedo (SSA), which summarizes the balance between absorption and scattering in a single amount-independent optical property. This balance, relative to the reflectance of the underlying surface, determines whether the SW aerosol–radiation interaction produces positive or negative forcing at the TOA, whereas the dust amount mainly scales its magnitude (Claquin et al., 1998; Myhre and Stordal, 2001; Haugvaldstad et al., 2025). We therefore take the SW effective radiative forcing due to aerosol–radiation interactions (hereafter ERF_{ari}^{SW}) as our target, and SSA as the optical property that governs its sign.

This relationship between SSA and SW forcing provides a basis for an emergent constraint. Across a model ensemble, if the spread in forcing is systematically related to an observable dust property, observations of that property can be used to identify the part of the modeled forcing range that is most consistent with the real atmosphere. For Saharan dust, such a constraint is feasible because observational estimates of dust absorption are available from Aerosol Robotic Network (AERONET) inversion products, which retrieve aerosol absorption and SSA from sun and sky radiance measurements, and from laboratory measurements (Di Biagio et al., 2019). This approach links forcing uncertainty to a measurable optical property and provides a way to evaluate model parameterizations of dust absorption and scattering. We therefore ask how much of the Saharan SW dust-forcing spread can be explained by SSA, where the observed SSA falls within the modeled range, and what forcing range is supported by this observational constraint.

Because dust forcing is spatially inhomogeneous, its climatic impacts are expected to be strongest near major source regions and along their transport pathways. The Sahara is by far the largest dust source on Earth, and the atmosphere above and downstream of this source region is therefore especially sensitive to the absorptive properties of mineral dust. Absorbing dust heats the overlying atmosphere, and this diabatic heating can modify the lower-tropospheric thermal structure and intensify the thermally driven surface low over the Sahara, the Saharan heat low (SHL), which organizes the low-level circulation of the West African monsoon (WAM) (Lavaysse et al., 2009). Changes in SHL intensity can alter the monsoon flow and the associated moisture transport into the Sahel, thereby affecting regional precipitation. Single-model studies have shown that this Sahel precipitation response is highly sensitive to the absorbing properties of dust, with more absorbing dust favouring increased monsoon rainfall (Solmon et al., 2008; Strong et al., 2015). Thus, uncertainty in dust absorption is not only a problem for estimating global radiative forcing, but also a source of uncertainty in regional monsoon responses.

An experiment in which the amount of dust emissions is doubled has recently been analyzed in this context by Haugvaldstad et al. (2025). They characterized the dust effective radiative forcing (ERF) across the nine ESMs participating in the Aerosol Chemistry Model Intercomparison Project (AerChemMIP)

https://doi.org/10.5194/egusphere-2026-6804
Preprint. Discussion started: 12 November 2026
© Author(s) 2026. CC BY 4.0 License.

and decomposed it into contributions from aerosol–radiation interactions and cloud adjustments. Their analysis showed that differences in dust absorptivity dominate the spread in $\mathbf{ERF}_{\mathbf{ari}}^{\mathbf{SW}}$ and that constraints on dust optical depth alone are insufficient. They therefore called for a broader set of observational constraints on the dust properties that shape the forcing, including its refractive index. Building on this forcing-focused analysis, we use the SSA constraint introduced above and examine whether the same absorption-related spread also projects onto the downstream WAM response. Although the link between dust absorption and Sahel rainfall has been examined in single-model studies (Solmon et al., 2008; Strong et al., 2015), and Haugvaldstad et al. (2025) diagnosed the global precipitation response through an energetic argument, the multi-model pathway from Saharan SW forcing to WAM circulation and rainfall has not been established. We examine how this pathway develops from the SW forcing to changes in regional circulation and rainfall. To connect the forcing to the underlying scattering and absorption processes, we separate the SW dust forcing into its scattering and absorption components using the approximate partial radiative perturbation method (APRP, Taylor et al., 2007). APRP relies on standard radiative flux outputs, allowing a consistent decomposition across all models, whereas the aerosol-free radiation diagnostics used by Haugvaldstad et al. (2025) are available only for a subset of models.

This study uses simulations in which dust emissions are doubled, together with the corresponding control simulations, from the CMIP6 ESMs participating in AerChemMIP. All dynamical and precipitation diagnostics are performed for boreal summer (JJA), when Saharan dust loading and the West African monsoon both reach their seasonal peak. The remainder of the paper is organized around the link between Saharan dust SSA, SW dust forcing, and the regional monsoon response. Section 2 introduces the model ensemble and observational basis for evaluating Saharan dust SSA. Section 3 first examines how SSA explains the spread in SW dust forcing and constrains its plausible range. It then connects SSA-related absorption to the Saharan heat low, monsoon inflow, Sahel rainfall, and the cloud-radiative response over the Sahel. Section 4 summarizes the main findings and discusses their implications. By linking SSA to both Saharan dust forcing and the downstream monsoon response, this study highlights the need to constrain not only how much dust models simulate, but also how absorptive that dust is.

2 Data and methods

2.1 AerChemMIP experiments, model ensemble, and evaluation datasets

We analyze the piClim-2xdust and piClim-control experiments of AerChemMIP (Collins et al., 2017). Both experiments prescribe sea surface temperatures (SSTs) and sea ice at pre-industrial 1850 conditions, with anthropogenic aerosol emissions and greenhouse gas concentrations also fixed at 1850 levels. In

https://doi.org/10.5194/egusphere-2026-6804
Preprint. Discussion started: 12 November 2026
© Author(s) 2026. CC BY 4.0 License.



piClim-2xdust, the dust-emission scaling factor applied to the interactive dust emission scheme in each model is doubled, while piClim-control is otherwise identical except that this scaling factor remains unperturbed. We define the perturbation response throughout as $\Delta X = X^{2xdust} - X^{ctrl}$, where X^{2xdust} and X^{ctrl} denote the 30-year climatologies of piClim-2xdust and piClim-control, respectively. This difference isolates the rapid response to the imposed dust-emission perturbation. Because dust emission remains computed online from surface wind and land-surface conditions, doubling the emission tuning factor does not necessarily double the emitted dust mass in each model. The realized increase ranges from about 70 % to 105 % across the ensemble (Haugvaldstad et al., 2025). Because SSTs are prescribed, the simulated responses represent rapid adjustments to the dust forcing, and exclude slower responses mediated by changes in surface temperature. The implications of this constraint for the monsoon response are discussed in Sect. 4.

Nine CMIP6 ESMs participated in the experiment. We analyze eight of these models, MIROC6, NorESM2-LM, EC-Earth3-AerChem, MPI-ESM-1-2-HAM, CNRM-ESM2-1, IPSL-CM6A-LR-INCA, UKESM1-0-LL, and GFDL-ESM4. GISS-E2-1-G is excluded because its reported absorption diagnostic implies an unphysical column SSA of about 0.08 (Sect. 2.3). Consequently, the main SSA-based forcing, monsoon, and emergent-constraint analyses are based on eight models. All model output was obtained from the Earth System Grid Federation (ESGF), and the variant labels are listed in the Code and data availability section. Each model provides at least 30 years of simulation, all of which are retained for the climatological analysis. Because the experiments use prescribed SSTs and piClim-2xdust is branched from an equilibrated control, we treat the response as a rapid adjustment to the imposed dust-emission perturbation and do not exclude a spin-up period. Haugvaldstad et al. (2025, Table 1) provide details of the individual models, including their dust emission schemes, particle size representations, and refractive indices. They also analyzed the same ensemble for the global dust effective radiative forcing. The present study builds on that analysis by focusing on the ERF^{SW}_{ari} over North Africa and its dynamical propagation into the West African monsoon, using the Saharan column SSA (Sect. 2.3) as the key diagnostic of model dust absorptivity.

To evaluate the present-day West African mean state simulated by the same models, we also analyze CMIP6 historical simulations and compare them with observational products for precipitation and aerosol optical depth (AOD). This evaluation complements the idealized piClim analysis. The piClim experiments isolate the rapid response to a dust-emission perturbation, whereas the historical comparison assesses whether the models reproduce the observed climatological fields on which the regional response acts. The historical comparisons are performed for boreal summer, June-July-August (JJA), and all fields are regridded to a common 1° × 1° grid before analysis.

https://doi.org/10.5194/egusphere-2026-6804
Preprint. Discussion started: 12 November 2026
© Author(s) 2026. CC BY 4.0 License.

Present-day monsoon precipitation is evaluated for 1995–2014 using two monthly observational products, GPCP version 3.3 and CHIRPS version 2.0. These products combine observational information in different ways, with GPCP based on a satellite-gauge merged approach and CHIRPS based on station-blended infrared precipitation estimates. Using both products provides an estimate of observational uncertainty in the West African rainfall climatology. Present-day dust loading is evaluated using 550 nm AOD from MODIS Aqua (the combined Dark Target–Deep Blue land-and-ocean product) and MISR (the Level 3 Component Global Aerosol product, MIL3DAEN version 004, monthly 0.5° × 0.5° aggregation). Because reliable satellite AOD retrievals are available only from the early 2000s, both products are evaluated over 2003–2014 rather than over the full 1995–2014 period. MODIS Aqua is based on the target 1° × 1° grid, while MISR is conservatively regridded from 0.5° to 1° to preserve area-integrated AOD. As with precipitation, using two products with different sampling and retrieval algorithms brackets the observational uncertainty in the dust field.

2.2 Radiative forcing decomposition

We decompose the TOA radiative responses into SW aerosol–radiation, SW aerosol–cloud, surface-albedo, and LW components. We refer to these responses as *effective* radiative forcings because they include both the instantaneous radiative perturbation from the imposed dust-emission change and the rapid atmospheric adjustments that occur under prescribed SSTs and sea ice. For the SW terms, we use the APRP method of Taylor et al. (2007), following the implementation of Zelinka et al. (2014). APRP diagnoses changes in planetary albedo from standard monthly radiative fluxes and separates the response into surface-albedo, non-cloud atmospheric, and cloud-mediated terms. The APRP term grouping and implementation used in this study are given in Appendix A.

In this study, the non-cloud atmospheric terms are used to define $\mathrm{ERF}^{\mathrm{SW}}_{\mathrm{ari}}$, while the cloud-mediated terms are used to define the SW forcing due to aerosol–cloud interactions, $\mathrm{ERF}^{\mathrm{SW}}_{\mathrm{aci}}$. The surface-albedo terms are retained separately as $\mathrm{ERF}^{\mathrm{SW}}_{\mathrm{alb}}$. This decomposition is central to our analysis because it separates $\mathrm{ERF}^{\mathrm{SW}}_{\mathrm{ari}}$ into scattering and absorption components for all models using only standard archived radiative fluxes.

The LW forcings due to aerosol–radiation and aerosol–cloud interactions, $\mathrm{ERF}^{\mathrm{LW}}_{\mathrm{ari}}$ and $\mathrm{ERF}^{\mathrm{LW}}_{\mathrm{aci}}$, are diagnosed separately from the SW APRP decomposition following Zelinka et al. (2014), with the detailed definitions given in Appendix A. All radiative decompositions are computed from monthly model output and evaluated as piClim-2xdust minus piClim-control. The threshold treatment for small cloud fractions and the subsequent regridding procedure are also described in Appendix A.

https://doi.org/10.5194/egusphere-2026-6804
Preprint. Discussion started: 12 November 2026
© Author(s) 2026. CC BY 4.0 License.

2.3 Saharan column single-scattering albedo

We characterize model dust absorptivity using the column-integrated total-aerosol SSA at 550 nm over the Saharan domain. For each grid cell, SSA is computed from the standard CMIP6 aerosol optical diagnostics as

$$\omega_0 = 1 - \tau_{\mathrm{abs}}^{550}/\tau_{\mathrm{ext}}^{550},$$

where $\tau_{\mathrm{ext}}^{550}$ and $\tau_{\mathrm{abs}}^{550}$ denote total AOD and absorption AOD at 550 nm (CMIP6 variables of od550aer and abs550aer, respectively; Juckes et al., 2020). Because $\tau_{\mathrm{abs}}^{550}$ and $\tau_{\mathrm{ext}}^{550}$ are column integrals of layer optical depths, this quantity is the extinction-weighted column mean of the single-scattering albedo used in each model's optical properties. It does not include multiple scattering or reflection, which enter only the radiative transfer calculation of the forcing. We then calculate the Saharan column SSA, $\overline{\omega_0}^{\mathrm{Sah}}$, as the cosine-latitude-weighted mean of grid-cell SSA over the Saharan land mask.

A dust-specific absorption optical depth is not available as a standard AerChemMIP diagnostic for most models. However, under the pre-industrial aerosol conditions of the piClim experiments, mineral dust dominates the aerosol column over the Sahara. The total-aerosol column SSA therefore provides an effective proxy for Saharan dust SSA, following the same approach used for CMIP6 models by Mallet et al. (2021). This column-integrated diagnostic is also directly comparable to the columnar SSA retrieved from AERONET inversion products used for the observational constraint in Sect. 2.4.

As a consistency check, we compare the control-based Saharan column SSA with a perturbation-based SSA calculated from the incremental AODs between piClim-2xdust and piClim-control (Fig. S2). The two diagnostics closely follow the one-to-one relationship across the eight models. This supports the use of the control-based Saharan column SSA as the main diagnostic of dust absorptivity. We also test whether the regional SSA depends on the low-extinction threshold used when forming grid-cell SSA. Varying the $\tau_{\mathrm{ext}}^{550}$ threshold between 0.001 and 0.01 has negligible effect on the Saharan-mean SSA and does not change the model ordering, because the Saharan land mask is dominated by optically thick dust-laden grid cells (Appendix B).

On this basis, models are grouped by Saharan column SSA for the composite analyses in Sect. 3.3 and 3.4. The four higher-SSA models are classified as the High-SSA group (MIROC6, NorESM2-LM, EC-Earth3-AerChem, and MPI-ESM-1-2-HAM; SSA 0.957–0.976), and the four lower-SSA models as the Low-SSA group (GFDL-ESM4, CNRM-ESM2-1, UKESM1-0-LL, and IPSL-CM6A-LR-INCA; SSA 0.875–0.946). These labels are used only as a descriptive grouping for composite analysis. The emergent-

https://doi.org/10.5194/egusphere-2026-6804
Preprint. Discussion started: 12 November 2026
© Author(s) 2026. CC BY 4.0 License.

constraint regression in Sect. 2.4 treats SSA as a continuous model property.

GISS-E2-1-G is not included in the SSA-based analysis. Its reported absorption diagnostic gives a Saharan column SSA of approximately 0.08, far below the physically plausible range for atmospheric mineral dust, for which measured 550 nm SSA values generally exceed about 0.8 (Di Biagio et al., 2019). We therefore interpret this value as an inconsistency in the reported $\tau_{\mathrm{abs,aer}}^{550}$ diagnostic rather than as a representation of dust optical properties, and exclude GISS-E2-1-G from all analyses, leaving an eight-model ensemble.

2.4 Observational SSA constraint and emergent-constraint regression

We constrain the modeled Saharan column SSA using ground-based columnar retrievals from the AERONET network. We use Level 2.0 quality-assured inversion products at five stations within or bordering the Saharan dust domain: Tamanrasset, El Farafra, Ouarzazate, Bordj Badji Mokhtar, and Bodélé. AERONET inversion products retrieve aerosol optical properties from Sun and sky radiance measurements using established algorithms (Dubovik and King, 2000; Giles et al., 2019). The retrieval procedure and spectral interpolation are described in Appendix C.

AERONET reports SSA at 440, 675, 870, and 1020 nm. We interpolate these values to 550 nm and average the five station estimates , giving an observational constraint of SSA_obs = 0.9543 ± 0.0060 at 550 nm, where the uncertainty is the inter-station standard deviation and serves as a conservative measure of regional representativeness.

The emergent constraint relates the modeled Saharan $\mathrm{ERF}_{\mathrm{ari}}^{\mathrm{SW}}$ to the Saharan column SSA across the eight-model ensemble. We fit an ordinary least-squares regression of $\mathrm{ERF}_{\mathrm{ari}}^{\mathrm{SW}}$ on Saharan column SSA and use the AERONET-based observational constraint to infer the corresponding forcing range. The uncertainty propagation accounts for both the observational uncertainty in SSA and the predictive uncertainty of the regression. The regression formulation and Monte Carlo procedure are given in Appendix D. The resulting constrained forcing range is reported in Sect. 3.2.

2.5 Analysis domains, season, and monsoon diagnostics

Two regional domains are used for the regional analysis. The Sahara domain spans 15–35° N and 20° W–35° E, covering the main dust source and the Saharan Heat Low. The Sahel domain spans 0–15° N and 20° W–15° E, covering the West African monsoon rain belt. Regional means are calculated as cosine-

https://doi.org/10.5194/egusphere-2026-6804
Preprint. Discussion started: 12 November 2026
© Author(s) 2026. CC BY 4.0 License.

latitude-weighted area averages within each domain. Zonal-mean cross-section diagnostics use the 15° W–15° E longitude band indicated in the corresponding figures.

All circulation and precipitation diagnostics are evaluated for boreal summer, June–July–August (JJA), when the West African monsoon and the Saharan heat low are fully developed. The Saharan column SSA is the only exception. It is calculated as an annual-mean quantity, consistent with its interpretation as an intensive optical property and with the annual-mean observational constraint described in Sect. 2.4.

To examine how Saharan SW dust absorption is linked to the Sahel rainfall response, we define a set of regional perturbation diagnostics. Each diagnostic is calculated as the JJA-mean difference between piClim-2xdust and piClim-control and then averaged over the relevant domain.

Over the Sahara, we use four diagnostics. The clear-sky atmospheric shortwave absorption, $\Delta \mathrm{SW}_{\mathrm{abs}}$, is defined as the changes in clear-sky net SW convergence between the TOA and the surface. Mid-tropospheric temperature, $\Delta T_{500-700}$, is averaged over the 500–700 hPa layer. The low-level atmospheric thickness is defined as $\mathrm{LLAT} = Z_{700} - Z_{925}$, where Z_{700} and Z_{925} are geopotential heights at 700 and 925 hPa, respectively. This quantity increases when the lower tropospheric column warms and expands. Sea-level pressure, Δpsl, is used as the surface-pressure signature of the Saharan heat low. LLAT and psl are hydrostatically linked diagnostics of heat-low intensity and are therefore interpreted as complementary measures rather than independent quantities.

Over the Sahel we use three diagnostics. The 850 hPa zonal wind, Δu_{850}, represents the low-level monsoon inflow. The mid-level pressure velocity, $\Delta \omega_{500-700}$, is averaged over the 500–700 hPa layer, with negative values denoting enhanced ascent. Precipitation, ΔP, represents the rainfall response. The zonal wind at 850 hPa is used because the southwesterly monsoon inflow opposes the climatological low-level easterly flow over the Sahel. A strengthening of the monsoon inflow therefore appears as an increase in u_{850}, corresponding to a weakening of the easterly component.

3 Results

3.1 Saharan dust SSA spread and present-day model evaluation

https://doi.org/10.5194/egusphere-2026-6804
Preprint. Discussion started: 12 November 2026
© Author(s) 2026. CC BY 4.0 License.

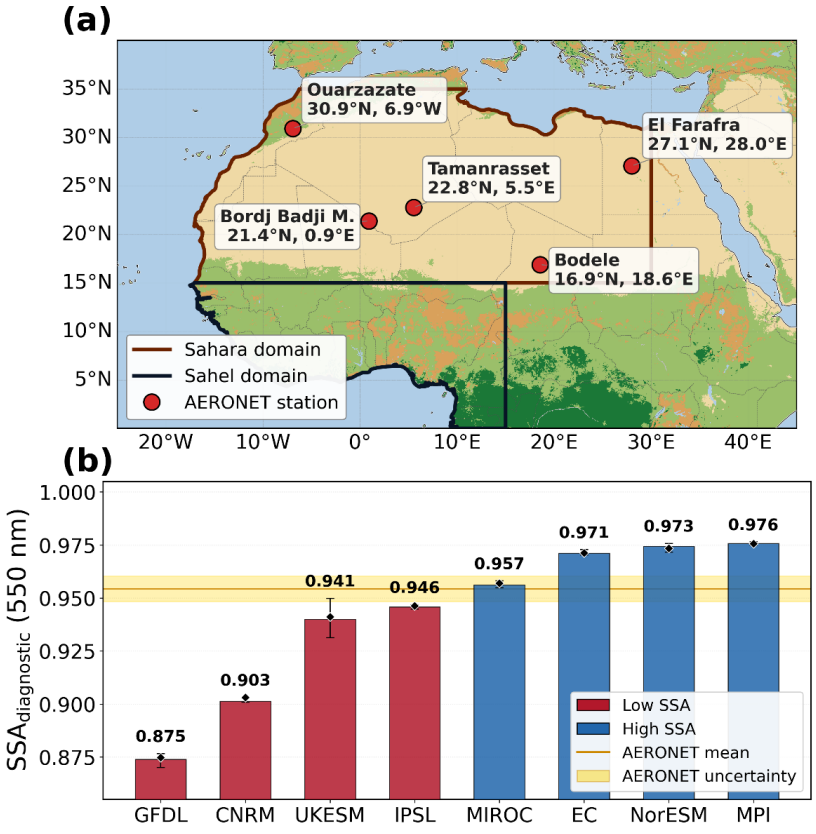


Figure 1. Saharan dust SSA and observational constraint. (a) Sahara and Sahel analysis domains over MODIS IGBP land cover, with the five AERONET stations used to derive the observational SSA constraint marked by red circles. (b) Sahara-mean column SSA at 550 nm for the eight CMIP6 models. Bars show the median, error bars show the 25th–75th percentile range, and diamonds show the mean. Bar colors distinguish the low- and high-SSA groups used for composite analyses. The red horizontal bar marks the AERONET mean SSA, and the yellow band denotes the AERONET-based observational constraint. Models are ordered by increasing SSA.

Figure 1a shows the Sahara and Sahel analysis domains together with the five AERONET stations used for the observational SSA constraint. Figure 1b shows the Saharan column SSA, $\overline{\omega_0}^{\mathrm{Sah}}$, for the eight analyzed models. The model spread is large, ranging from 0.875 in GFDL-ESM4 to 0.976 in MPI-ESM-1-2-HAM. This range spans strongly absorbing to nearly scattering dust regimes, indicating that the

https://doi.org/10.5194/egusphere-2026-6804
Preprint. Discussion started: 12 November 2026
© Author(s) 2026. CC BY 4.0 License.

models differ substantially in their representation of Saharan dust absorptivity.

The AERONET-based observational constraint, 0.9543 ± 0.0060, lies within the modeled range but not near its centre. Four models fall below the observed range, GFDL-ESM4, CNRM-ESM2-1, UKESM1-0-LL, and IPSL-CM6A-LR-INCA, indicating dust that is more absorbing than the observational estimate. Three models fall above the observed range, EC-Earth3-AerChem, NorESM2-LM, and MPI-ESM-1-2-HAM, indicating dust that is more scattering than the observational estimate. Only MIROC6 lies within the observed range. The observed SSA therefore separates the ensemble into models that are too absorbing and models that are too scattering, rather than revealing a common bias shared by all models.

This interpretation is supported by an internal consistency check using our in-house UKESM1 configuration, in which the dust-only SSA can be calculated directly from the model-internal Mie optical properties. We compare this Mie-calculated dust SSA with the CMIP6 model-output aerosol SSA used in this study (Fig. S1). The Mie-calculated dust SSA varies only weakly across the Saharan grid boxes, whereas the model-output aerosol SSA shows a broader spread because it represents the total aerosol column and is therefore affected by the local dust fraction. To assess this effect, Fig. S1 compares all Saharan grid boxes with subsets increasingly dominated by dust, selected using the 25th, 50th, and 75th percentiles of the dust fraction, defined as $\tau^{550}_{\mathrm{ext,dust}} / \tau^{550}_{\mathrm{ext,aer}}$. The model-output aerosol SSA is systematically higher than the Mie-calculated dust SSA, but this positive bias decreases as the analysis is restricted to more dust-dominated grid boxes. This tendency suggests that part of the offset arises from non-dust aerosol contributions to the total-aerosol SSA, while the reduced bias under dust-dominated conditions supports the use of the CMIP6 model-output SSA as an effective proxy for Saharan dust absorptivity. Nevertheless, this diagnostic should be interpreted as a total-aerosol column SSA rather than an exact dust-only optical property.

Before examining the dust-perturbed response, we evaluate the present-day summertime climatological mean state in the same models. Figure 2 compares JJA precipitation and Saharan AOD in the CMIP6 historical simulations against two observational products. The models generally reproduce the observed precipitation patterns (Fig. S3), with correlations of 0.74–0.94. However, most models overestimate the meridional rainfall contrast, consistent with known CMIP6 biases over West Africa (Fig. S3; Toolan et al., 2025). This bias affects the amplitude of the summertime rainfall climatology but does not substantially displace the rainband that is central to the mechanism examined below.

The present-day summertime Saharan AOD climatology is less consistently reproduced, as shown by large spread in spatial correlations with the MODIS observations (Fig. 2). NorESM2-LM shows a distinct spatial pattern, with excessive AOD in the eastern Sahara and too little AOD in the west (Fig. S4), so its

https://doi.org/10.5194/egusphere-2026-6804
Preprint. Discussion started: 12 November 2026
© Author(s) 2026. CC BY 4.0 License.

correlation with MODIS nearly vanishes. GFDL-ESM4 and IPSL-CM6A-LR-INCA overestimate Saharan AOD relative to observations, whereas most other models underestimate it. This discrepancy in the simulated summertime dust climatology is a known limitation of current CMIP6 dust simulations (Zhao et al., 2022; Gliß et al., 2021), and motivates the focus on SSA as an intensive optical property rather than on dust amount alone. The following subsection examines how this spread in Saharan dust absorptivity projects onto ERF_{ari}^{SW}.

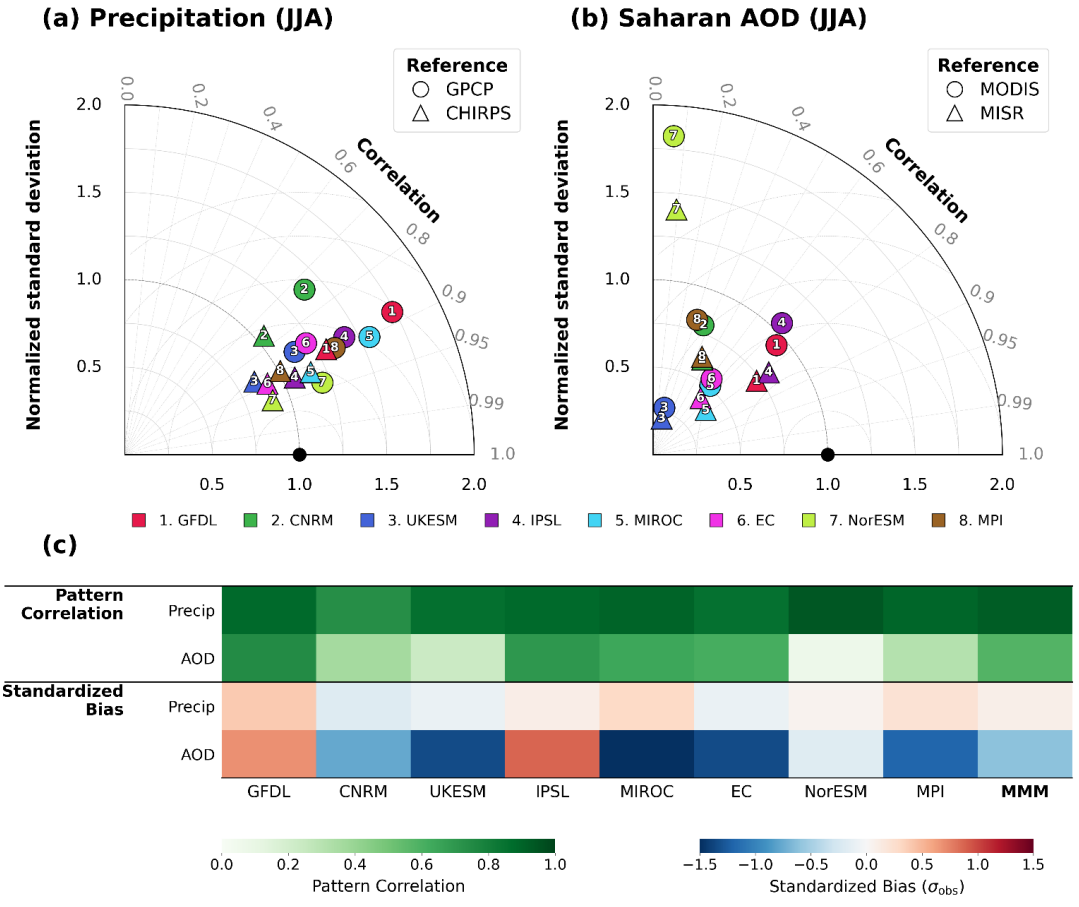


Figure 2. Present-day evaluation of West African precipitation and Saharan dust loading. (a) Taylor diagram of JJA-mean precipitation over West Africa (0–35° N, 20° W–35° E, land only) for CMIP6 historical simulations (1995–2014), evaluated against GPCP (circles) and CHIRPS (triangles). (b) As in (a) but for 550 nm AOD over the Sahara (15–35° N, 20° W–35° E), evaluated against MODIS (circles) and MISR (triangles) for 2003–2014. Marker shape denotes the reference dataset, and marker color and

https://doi.org/10.5194/egusphere-2026-6804
Preprint. Discussion started: 12 November 2026
© Author(s) 2026. CC BY 4.0 License.

number identify individual models. Standard deviations are normalized by that of the corresponding reference dataset, so the black dot marks the reference point for both datasets. (c) Pattern correlation (top) and standardized bias (bottom) of JJA-mean precipitation and Saharan AOD for each model and the multi-model mean (MMM), relative to GPCP precipitation and MODIS AOD. Standardized bias is defined as (model − observation)/σ_obs.

3.2 SSA control of Saharan SW forcing due to aerosol–radiation interactions

The spread in Saharan dust absorptivity is reflected directly in the representation of SW forcing by the models. The total dust ERF over West Africa shows substantial inter-model disagreement in both sign and magnitude (Fig. S5). The multi-model mean is weak and spatially heterogeneous, with positive values over parts of the Saharan interior and negative values over the Atlantic outflow region (Fig. S5a). Sign agreement is also limited over broad parts of North Africa, indicating that the models do not produce a robust forcing sign in this region. The inter-model standard deviation exceeds 3 W m^{-2} over large parts of the Saharan interior and is comparable to, or larger than, the multi-model mean response (Fig. S5b). An APRP variance decomposition shows that this spread is dominated by SW aerosol–radiation terms, with the largest contributions from SW aerosol absorption and SW aerosol scattering, whereas cloud-related, surface-albedo, and LW terms are comparatively small (Fig. S5c).

The model-by-model decomposition shows why the sign of ERF_{ari}^{SW} differs across the ensemble. Low-SSA models generally produce near-zero to positive Sahara land-mean ERF_{ari}^{SW}, ranging from +0.01 W m^{-2} in UKESM1-0-LL to +4.76 W m^{-2} in CNRM-ESM2-1 (Fig. S6). In contrast, all High-SSA models produce negative Sahara land-mean ERF_{ari}^{SW}, between −1.73 and −2.41 W m^{-2} (Fig. S6). This sign separation arises from the balance between scattering and absorption. Here, the scattering and absorption components are the APRP terms defined in Appendix A, which express the TOA SW flux change attributable to changes in atmospheric scattering and absorption, respectively. The absorption component is therefore a TOA quantity, distinct from the atmospheric SW absorption (TOA minus surface) used in Sect. 3.3. A positive absorption component indicates that enhanced dust absorption reduces the planetary albedo. The SW scattering component is negative in all models and therefore acts as a cooling term irrespective of SSA group (Fig. S7). The SW absorption component, however, differs strongly between the two groups. It is large and positive in the Low-SSA models, reaching +6.57 W m^{-2} in CNRM-ESM2-1 and +5.29 W m^{-2} in IPSL-CM6A-LR-INCA, but remains weak in the High-SSA models, from −0.09 to +1.05 W m^{-2} (Fig. S8). Thus, the Low-SSA models produce positive or near-zero net $\mathbf{ERF_{ari}^{SW}}$ because strong absorption offsets or exceeds scattering cooling, whereas the High-SSA models produce negative

https://doi.org/10.5194/egusphere-2026-6804
Preprint. Discussion started: 12 November 2026
© Author(s) 2026. CC BY 4.0 License.

forcing because weak absorption does not compensate for scattering cooling. Over the bright Saharan surface, this compensation is amplified by multiple reflections between the dust layer and the surface, because surface-reflected SW radiation passes through the absorbing layer again (Shell and Somerville, 2007). The APRP single-layer formulation explicitly accounts for this surface–atmosphere multiple reflection (Taylor et al., 2007), so the effect is contained in the absorption component.

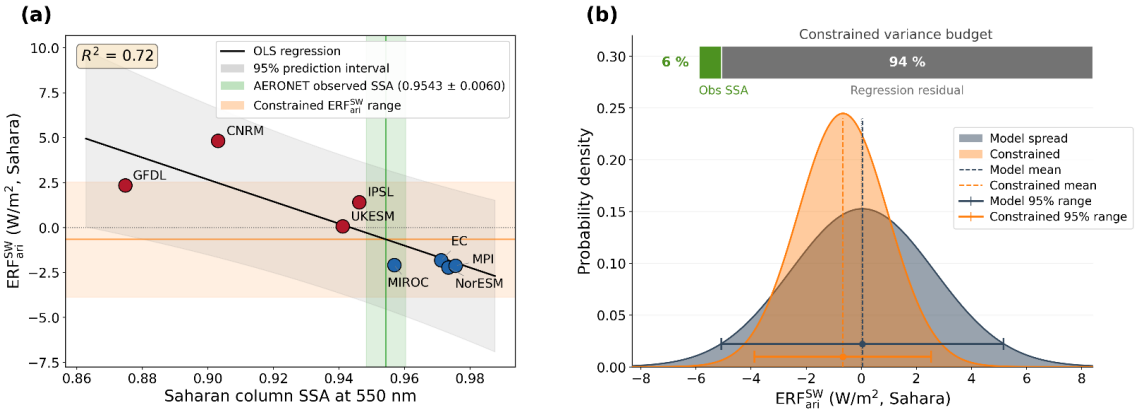


Figure 3. SSA-based emergent constraint on Saharan $\mathbf{ERF^{SW}_{ari}}$. (a) Sahara-mean dust single-scattering albedo at 550 nm versus Sahara-mean $\mathbf{ERF^{SW}_{ari}}$ across the eight analyzed CMIP6 models, with the ordinary least-squares regression and its 95 % prediction interval. The green band marks the AERONET-based observational SSA constraint, and the orange band marks the corresponding SSA-constrained range of $\mathbf{ERF^{SW}_{ari}}$. (b) Prior model distribution and SSA-constrained distribution of Sahara-mean $\mathbf{ERF^{SW}_{ari}}$. Vertical dashed lines indicate the corresponding means, and horizontal bars show the 95 % ranges. The inset variance decomposition shows the relative contributions of observational SSA uncertainty and regression residual uncertainty to the SSA-constrained distribution.

Figure 3a quantifies this dependence on Saharan column SSA. Across the eight analyzed models, Sahara-mean ERF^{SW}_{ari} decreases with increasing SSA, and a linear fit explains much of the inter-model spread ($R^2 = 0.72$). The lower-SSA, more absorbing models occupy the positive or weakly negative forcing side of the relationship, whereas the higher-SSA, more scattering models occupy the negative forcing side. This relationship confirms that the inter-model spread in Saharan $\mathbf{ERF^{SW}_{ari}}$ is primarily controlled by dust absorptivity rather than by scattering alone.

Because SSA is observable, this forcing spread can be constrained. The AERONET-based SSA constraint lies within the modeled SSA range (Fig. 3a). The resulting SSA-constrained distribution gives

https://doi.org/10.5194/egusphere-2026-6804
Preprint. Discussion started: 12 November 2026
© Author(s) 2026. CC BY 4.0 License.

a Sahara-mean ERF_{ari}^{SW} centered near −0.66 W m⁻², with a 95 % interval of −3.87 to +2.53 W m⁻² (Fig. 3b). Because this constrained interval still spans zero, the SSA-based emergent constraint narrows the plausible range of Saharan ERF_{ari}^{SW} but does not determine its sign at the 95 % level. The posterior distribution is narrower than the prior model spread, and the uncertainty decomposition shows that most of the remaining constrained variance is associated with regression residual uncertainty rather than observational SSA uncertainty (Fig. 3b). The relationship is, however, carried mainly by the contrast between the two SSA groups, with no model falling between them, and it is not resolved within either group, which contain only four models each. Because the AERONET constraint lies in this gap, the constrained estimate relies on the assumed linearity rather than being anchored by individual models.

The SSA–forcing relationship is not simply a consequence of differences in dust amount. The models show substantial spread in both background AOD and the imposed dust-induced AOD perturbation (Fig. S9). For example, IPSL-CM6A-LR-INCA has the largest piClim-control AOD and ΔAOD, while several High-SSA models also produce sizeable ΔAOD values (Fig. S9a,c). Similarly, AAOD and ΔAAOD are generally larger in the Low-SSA models, but their values still vary within each group (Fig. S9b,d). More directly, ΔAOD is essentially uncorrelated with Saharan SSA ($R^2 = 0.01$; Fig. S10b). By contrast, the forcing efficiency, defined as $\eta = ERF_{ari}^{SW}/\Delta AOD$, retains a strong dependence on SSA ($R^2 = 0.71$; Fig. S10a). This confirms that the emergent relationship in Fig. 3 is primarily an optical-property constraint rather than a constraint on the magnitude of the dust optical-depth perturbation.

3.3 Dynamical pathway from Saharan absorption to Sahel rainfall

https://doi.org/10.5194/egusphere-2026-6804
Preprint. Discussion started: 12 November 2026
© Author(s) 2026. CC BY 4.0 License.

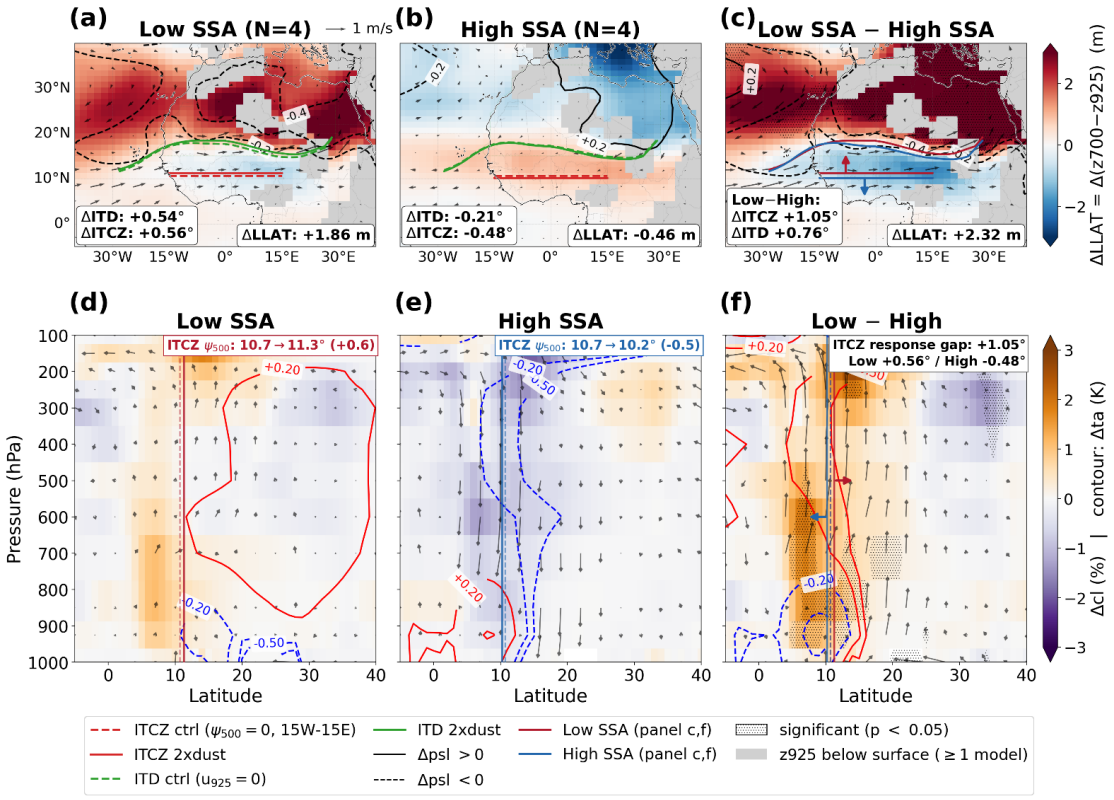


Figure 4. SSA-dependent heat-low and monsoon circulation response. Low-SSA more absorbing composite (a, d), High-SSA more scattering composite (b, e), and Low−High difference (c, f) of the West African monsoon response. (a)–(c) Changes in lower-tropospheric atmospheric thickness, $\Delta\mathrm{LLAT} = \Delta(Z_{700} - Z_{925})$, shown by shading, sea-level pressure by contours, and 1000–850 hPa winds by vectors. The green line denotes the intertropical discontinuity (ITD), and the red line denotes the intertropical convergence zone (ITCZ). (d)–(f) Zonal-mean cross-sections averaged over 15° W–15° E, showing cloud-fraction change by shading, temperature change by contours, and the anomalous meridional overturning circulation by vectors (Δv, $-\Delta\omega$). In (c) and (f), stippling marks Low−High differences significant at the 95 % level based on a permutation test. Grey shading indicates regions where the 925 hPa level lies below the surface in at least one model.

Having established that SSA controls the sign and magnitude of Saharan $\mathbf{ERF}^{\mathbf{SW}}_{\mathbf{ari}}$, we next examine how this optical difference propagates into the West African monsoon circulation. SSA sets the fraction of dust extinction that is absorbed rather than scattered, but the absorbed SW energy also depends on the

https://doi.org/10.5194/egusphere-2026-6804
Preprint. Discussion started: 12 November 2026
© Author(s) 2026. CC BY 4.0 License.

dust optical-depth perturbation, its vertical distribution, and the surface albedo beneath it. Thus, for a comparable increase in dust optical depth, lower SSA implies that a larger fraction of the extinguished SW radiation is absorbed, while higher SSA implies that a larger fraction is scattered. In the model ensemble, the atmospheric SW absorption response reflects both dust amount and dust absorptivity, while the systematic Low-SSA and High-SSA contrast highlights the role of absorptivity in shaping the monsoon response.

Figure 4 compares the Low-SSA and High-SSA composites, together with their difference, for lower-tropospheric thickness, sea-level pressure, low-level winds, ITD, ITCZ, cloud fraction, temperature, and overturning circulation. The Low-SSA group shows stronger warming-induced expansion of the lower troposphere over the Sahara, consistent with more efficient SW absorption by the dust perturbation. This response is accompanied by lower sea-level pressure over the Saharan interior and enhanced low-level monsoon inflow from the south and southwest. In contrast, the High-SSA group shows a weaker and more spatially limited heat-low and monsoon-flow response. The Low−High difference highlights a coherent heat-low contrast, with stronger lower-tropospheric thickening, lower Saharan pressure, and enhanced cyclonic low-level circulation over North Africa.

The ITD and ITCZ shifts are consistent with this circulation response. In the Low-SSA group, both boundaries move northward, whereas in the High-SSA group they tend to shift southward or respond more weakly. This contrast indicates that, when dust emissions are increased, more absorbing dust deepens the Saharan heat low and draws the monsoon convergence zone farther north, whereas more scattering dust produces a weaker or opposite monsoon response (Fig. 4a–c). This northward displacement is consistent with observational evidence that summertime Saharan dust outbreaks are accompanied by a northward shift of the Atlantic ITCZ (Wilcox et al., 2010), and with model simulations in which Saharan dust shifts the ITCZ northward and enhances the West African monsoon (Pan et al., 2018).

The vertical structure further supports this interpretation. In the Low-SSA composite, the zonal-mean cross-section shows warming over the Sahara and enhanced ascent near the Sahel rainband, together with a northward displacement of the low-level convergence and upper-level outflow structure (Fig. 4d). The High-SSA composite shows a weaker and more southward-confined response (Fig. 4e). The Low−High difference emphasizes this contrast, with stronger ascent and increased cloud fraction near the northern side of the climatological rainband (Fig. 4f). These results show that the dust-emission perturbation produces contrasting monsoon-circulation tendencies in the two SSA groups. The Low-SSA group shows monsoon strengthening, while the High-SSA group shows monsoon weakening or a reduced response. This contrast is also evident in the model-by-model precipitation response (Fig. S11). All Low-SSA

https://doi.org/10.5194/egusphere-2026-6804
Preprint. Discussion started: 12 November 2026
© Author(s) 2026. CC BY 4.0 License.

models show a positive change in the Sahel rain-band area under the dust-emission perturbation, whereas all High-SSA models show a negative change. Thus, the composite precipitation contrast in Fig. 4 reflects a systematic difference between the absorbing and scattering dust groups.

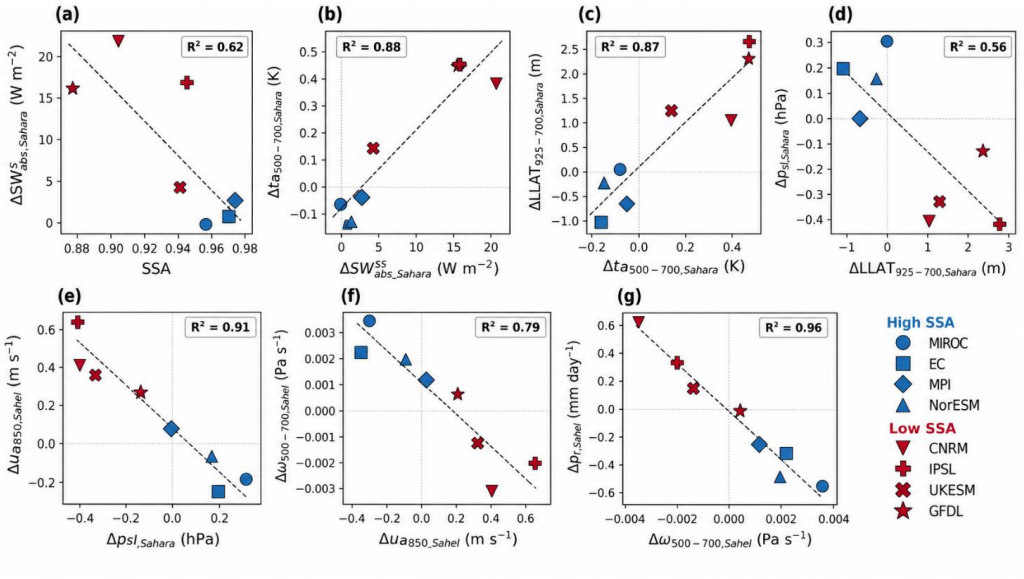


Figure 5. Inter-model pathway from Saharan dust absorption to Sahel rainfall. Each panel shows one step in the proposed response chain across the eight analyzed CMIP6 models: (a) Saharan column SSA versus clear-sky atmospheric SW absorption over the Sahara, (b) SW absorption versus 500–700 hPa temperature, (c) temperature versus lower-tropospheric atmospheric thickness, (d) thickness versus sea-level pressure, (e) Saharan sea-level pressure versus Sahel 850 hPa zonal wind, (f) Sahel 850 hPa zonal wind versus 500–700 hPa pressure velocity, and (g) pressure velocity versus precipitation. Red and blue markers denote Low-SSA and High-SSA models, respectively, with marker shapes identifying individual models. Dashed lines show ordinary least-squares fits, and R^2 values are shown in each panel. Positive Δu_{850} indicates stronger monsoon inflow, and negative $\Delta \omega_{500-700}$ indicates stronger ascent.

Figure 5 tests whether this pathway also appears across individual models. The inter-model relationships follow the expected sequence. Lower Saharan column SSA is associated with stronger clear-sky atmospheric SW absorption over the Sahara because lower SSA corresponds to a larger absorption fraction of aerosol extinction. Stronger SW absorption is then associated with warmer mid-tropospheric temperatures, and this warming is linked to increased lower-tropospheric atmospheric thickness. The thickness increase is associated with lower Saharan sea-level pressure, consistent with hydrostatic

https://doi.org/10.5194/egusphere-2026-6804
Preprint. Discussion started: 12 November 2026
© Author(s) 2026. CC BY 4.0 License.

deepening of the Saharan heat low. The pressure response is then linked to stronger Sahel low-level monsoon inflow, enhanced mid-tropospheric ascent, and increased Sahel precipitation.

Most links in this sequence show strong inter-model relationships, indicating that the models are ordered along a common physical pathway rather than responding independently at each step (Fig. 5). The first link, between SSA and SW absorption, is weaker than the downstream links because SW absorption is controlled by both the amount of added dust and its absorptivity. However, once the SW absorption anomaly is established, the subsequent thermodynamic, dynamic, and precipitation responses are highly coherent. These results collectively show that the rainfall response is not controlled by dust loading alone, but by how dust absorptivity regulates Saharan atmospheric heating, the Saharan heat low, and the associated monsoon circulation.

3.4 Cloud-radiative response and propagation of the forcing constraint

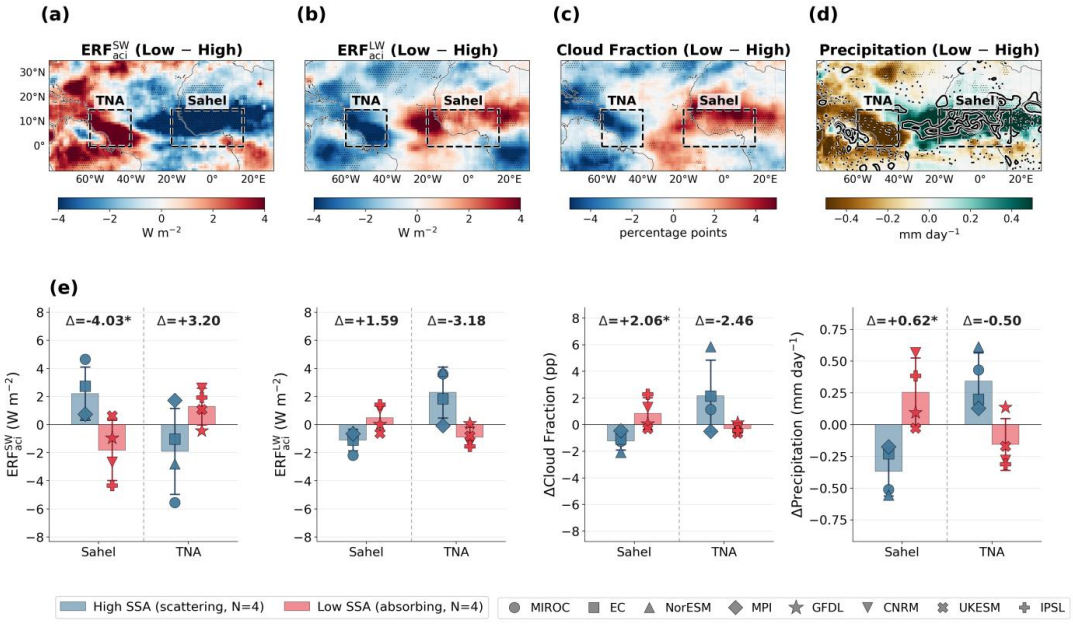


Figure 6. SSA-dependent cloud-radiative and precipitation response. Low−High SSA composite differences in (a) $\mathbf{ERF^{SW}_{aci}}$, (b) $\mathbf{ERF^{LW}_{aci}}$, (c) cloud fraction, and (d) precipitation. Contours in (d) show the 850 hPa moisture-flux convergence response. Stippling marks differences significant at the 95 % level based on a permutation test. (e) Regional-mean responses over the Sahel (0–15° N, 20° W–15° E) and

https://doi.org/10.5194/egusphere-2026-6804
Preprint. Discussion started: 12 November 2026
© Author(s) 2026. CC BY 4.0 License.

tropical North Atlantic (TNA; 0–15° N, 60–40° W) for High-SSA and Low-SSA groups. Bars show group means, symbols show individual models, and $\boldsymbol{\Delta}$ denotes the Low−High difference. Asterisks indicate statistically significant Low−High differences. Red and blue colors denote Low-SSA and High-SSA groups, respectively.

The SSA-dependent monsoon response is accompanied by a systematic cloud-radiative adjustment. Figure 6 shows the Low−High SSA difference in $\mathbf{ERF}_{\mathbf{aci}}^{\mathbf{SW}}$, $\mathbf{ERF}_{\mathbf{aci}}^{\mathbf{LW}}$, cloud fraction, and precipitation. Over the Sahel, the Low-SSA group shows increased cloud fraction and precipitation relative to the High-SSA group, together with a more negative $\mathbf{ERF}_{\mathbf{aci}}^{\mathbf{SW}}$ (Fig. 6a,c,d). This pattern is consistent with the dynamical pathway identified in Sect. 3.3, in which stronger Saharan absorption deepens the Saharan heat low, enhances monsoon inflow, and strengthens ascent over the Sahel. The resulting increase in cloudiness enhances SW reflection and produces a negative SW cloud-radiative response.

The regional-mean diagnostics confirm that the Sahel response is the most robust component of the cloud adjustment. The Low-SSA group produces a more negative Sahel $\mathbf{ERF}_{\mathbf{aci}}^{\mathbf{SW}}$, increased cloud fraction, and increased precipitation relative to the High-SSA group (Fig. 6e). Over the Sahel, the Low−High difference in $\mathbf{ERF}_{\mathbf{aci}}^{\mathbf{SW}}$ (−4.03 W m^{-2}) is significant and about 2.5 times larger in magnitude than the opposing, non-significant LW difference (+1.59 W m^{-2}). The net cloud-radiative adjustment over the Sahel is therefore negative and dominated by enhanced SW reflection from the increased cloud cover. Over the tropical North Atlantic, the response tends to have the opposite sign. The Low-SSA group shows reduced cloud fraction and precipitation, together with a more positive SW cloud-radiative response relative to the High-SSA group. Over the TNA, however, the SW (+3.20 W m^{-2}) and LW (−3.18 W m^{-2}) differences nearly cancel, so the dipole is expressed in the SW component rather than in the net cloud-radiative response. These TNA regional-mean differences are less robust than those over the Sahel, but their opposite sign indicates that the response is not confined to the continental rainband. Instead, it extends westward into the tropical Atlantic as part of a broader monsoon-cloud adjustment.

https://doi.org/10.5194/egusphere-2026-6804
Preprint. Discussion started: 12 November 2026
© Author(s) 2026. CC BY 4.0 License.

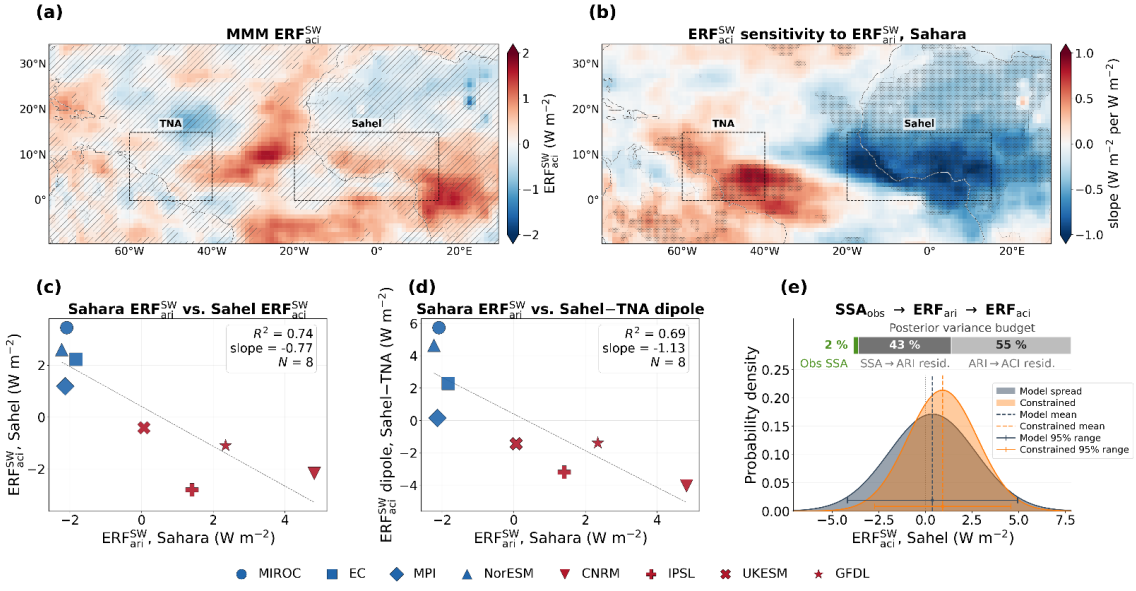


Figure 7. Propagation of the SSA constraint to the Sahel SW cloud-radiative response. (a) Multi-model mean ERF^{SW}_{aci}. Hatching marks regions where fewer than six of eight models agree on the sign. (b) Inter-model regression slope of local ERF^{SW}_{aci} against Sahara-mean ERF^{SW}_{ari}. Stippling marks slopes significant at the 95 % level (two-tailed t test, df = 6, uncorrected for field significance). (c) Sahara-mean ERF^{SW}_{ari} versus Sahel-mean ERF^{SW}_{aci}. (d) Sahara-mean ERF^{SW}_{ari} versus the Sahel–TNA dipole of ERF^{SW}_{aci}. Dashed lines in (c) and (d) show ordinary least-squares fits. (e) Prior model distribution and SSA-constrained distribution of Sahel-mean ERF^{SW}_{aci}. The variance bar shows contributions from observational SSA uncertainty, the SSA-to-ERF^{SW}_{ari} relationship, and the ERF^{SW}_{ari}-to-ERF^{SW}_{aci} relationship.

Figure 7 examines whether this cloud-radiative adjustment is organized by the SSA-controlled Saharan $\mathbf{ERF^{SW}_{ari}}$. The multi-model mean $\mathbf{ERF^{SW}_{aci}}$ shows weak sign agreement over broad parts of West Africa and the tropical North Atlantic (Fig. 7a). This indicates that the raw ensemble mean alone does not provide a robust sign or spatial structure of the SW cloud-radiative response. However, the local regression of $\mathbf{ERF^{SW}_{aci}}$ against Sahara-mean $\mathbf{ERF^{SW}_{ari}}$ reveals a clearer structure, with negative sensitivity over the Sahel and positive sensitivity over parts of the tropical North Atlantic (Fig. 7b). Models with more positive Saharan $\mathbf{ERF^{SW}_{ari}}$ therefore tend to produce stronger negative SW cloud-radiative response over the Sahel and an opposite-signed response over the Atlantic.

The regional regressions support this interpretation. Sahara-mean $\mathbf{ERF^{SW}_{ari}}$ explains a large fraction of the

https://doi.org/10.5194/egusphere-2026-6804
Preprint. Discussion started: 12 November 2026
© Author(s) 2026. CC BY 4.0 License.

inter-model spread in Sahel $\mathbf{ERF_{aci}^{SW}}$ (Fig. 7c). The same relationship holds for the Sahel–TNA $\mathbf{ERF_{aci}^{SW}}$ dipole (Fig. 7d), which we present as a robustness check rather than as independent evidence, because the two predictands are highly correlated across the ensemble. Thus, although the ACI response is diverse in the raw ensemble, much of its spatial contrast is organized by the SSA-controlled Saharan $\mathbf{ERF_{ari}^{SW}}$. This result links the local dust optical property to a downstream cloud-radiative response through the circulation pathway developed in Sect. 3.3. As for the SSA–forcing relationship in Fig. 3, this regression is carried mainly by the contrast between the two SSA groups. Within the High-SSA group, Sahel $\mathbf{ERF_{aci}^{SW}}$ shows little dependence on Sahara $\mathbf{ERF_{ari}^{SW}}$, so the relationship is better interpreted as a contrast between dust-absorption regimes than as a continuous sensitivity. Moreover, the constrained Sahara-mean $\mathbf{ERF_{ari}^{SW}}$ lies between the two groups, so the second propagation step also interpolates across a range not sampled by any model.

The emergent constraint in Fig. 7e is applied through a two-step propagation. First, the AERONET-based SSA constraint is used to constrain Sahara-mean $\mathbf{ERF_{ari}^{SW}}$, as described in Sect. 3.2. The resulting constrained $\mathbf{ERF_{ari}^{SW}}$ distribution is then passed through the inter-model regression between Sahara $\mathbf{ERF_{ari}^{SW}}$ and Sahel $\mathbf{ERF_{aci}^{SW}}$, with regression residual uncertainty included in the prediction. This approach constrains the Sahel cloud-radiative response through the physically motivated pathway from $\mathbf{SSA_{obs}}$ **to** $\mathbf{ERF_{ari}^{SW}}$, and to $\mathbf{ERF_{aci}^{SW}}$, rather than by directly regressing Sahel cloud forcing on SSA alone.

The variance decomposition in Fig. 7e is calculated from the same Monte Carlo framework. The posterior variance is separated into contributions from observational SSA uncertainty, the SSA-to-$\mathbf{ERF_{ari}^{SW}}$ regression residual, and the $\mathbf{ERF_{ari}^{SW}}$-to-$\mathbf{ERF_{aci}^{SW}}$ regression residual. The observational SSA uncertainty contributes only a small fraction of the posterior variance, while most of the remaining uncertainty comes from the two regression residual terms (Fig. 7e). This indicates that the limiting uncertainty is not the precision of the AERONET SSA estimate, but the model spread in how Saharan dust absorption is converted into $\mathbf{ERF_{ari}^{SW}}$ and then into cloud-radiative adjustment.

The SSA-constrained distribution of Sahel $\mathrm{ERF_{aci}^{SW}}$ is narrower than the prior model distribution, but it still spans zero (Fig. 7e). Therefore, the observational SSA constraint reduces the plausible range of the Sahel SW cloud-radiative response but does not determine its sign. This result reinforces the central interpretation of this study. Saharan SSA constrains the partitioning of dust extinction into scattering and absorption, which organizes the Saharan $\mathbf{ERF_{ari}^{SW}}$, the heat-low and monsoon response, and part of the downstream cloud-radiative adjustment. However, the final Sahel ACI response also depends on model differences in circulation-cloud coupling and cloud-radiative processes, which remain important sources of uncertainty.

https://doi.org/10.5194/egusphere-2026-6804
Preprint. Discussion started: 12 November 2026
© Author(s) 2026. CC BY 4.0 License.

4 Summary and conclusions

Saharan dust single-scattering albedo is an observable intensive optical property that characterizes how efficiently dust extinction is partitioned into scattering and absorption. In this study, we used the AerChemMIP piClim-2xdust ensemble to examine how this optical property organizes the response to an idealized dust-emission perturbation. We focused on the physical and dynamical pathways from Saharan $\mathbf{ERF}_{\mathbf{ari}}^{\mathbf{SW}}$, through the Saharan heat low and West African monsoon circulation, to the downstream SW cloud-radiative response over the Sahel and tropical North Atlantic. This framework allows us to ask how far an observational constraint on dust absorptivity can propagate through a coupled forcing, circulation, and cloud-response system.

The first result is that Saharan column SSA strongly organizes the local $\mathbf{ERF}_{\mathbf{ari}}^{\mathbf{SW}}$. Across the eight models, Sahara-mean $\mathrm{ERF}_{\mathrm{ari}}^{\mathrm{SW}}$ decreases systematically with increasing SSA. An APRP decomposition further shows that this spread is controlled mainly by the SW scattering and absorption components, rather than by cloud-mediated or LW terms. Lower-SSA models produce stronger atmospheric absorption and near-zero to positive $\mathbf{ERF}_{\mathbf{ari}}^{\mathbf{SW}}$ over the bright Saharan surface, whereas higher-SSA models produce more negative $\mathbf{ERF}_{\mathbf{ari}}^{\mathbf{SW}}$ dominated by scattering. Applying the AERONET-based SSA constraint gives a constrained Sahara-mean $\mathrm{ERF}_{\mathrm{ari}}^{\mathrm{SW}}$ centered near zero, at −0.66 W m^{-2}, with a 95 % interval of −3.87 to +2.53 W m^{-2}. This constraint narrows the plausible range of Saharan $\mathbf{ERF}_{\mathbf{ari}}^{\mathbf{SW}}$ but does not determine its sign. The relationship is not simply a dust-loading effect, because the dust-induced AOD perturbation is weakly related to SSA, whereas SW forcing efficiency depends strongly on SSA.

The second result is that the SSA-dependent $\mathbf{ERF}_{\mathbf{ari}}^{\mathbf{SW}}$ is linked to a coherent monsoon circulation response. SSA sets the fraction of dust extinction that is absorbed, while the absorbed energy also depends on the dust optical-depth perturbation and the underlying surface. For a given perturbation, lower SSA therefore increases the absorbed fraction of the extinguished SW radiation, while higher SSA increases the scattered fraction. In the Low-SSA group, stronger Saharan absorption warms and expands the lower troposphere, deepens the Saharan heat low, strengthens low-level monsoon inflow, enhances Sahel ascent, and favors increased precipitation. In the High-SSA group, the weaker absorption response leads to a weaker or opposite monsoon tendency. Thus, the same dust-emission perturbation produces contrasting monsoon responses depending on dust absorptivity. The inter-model pathway therefore indicates that dust absorptivity helps organize the simulated West African monsoon response.

Although the raw SW cloud-radiative response lacks robust sign agreement across the ensemble, it

https://doi.org/10.5194/egusphere-2026-6804
Preprint. Discussion started: 12 November 2026
© Author(s) 2026. CC BY 4.0 License.

becomes more coherent when conditioned on Saharan dust absorptivity and $\mathbf{ERF}_{\mathbf{ari}}^{\mathbf{SW}}$. The multi-model mean ERF_{aci}^{SW} shows weak sign agreement over much of West Africa and the tropical North Atlantic, indicating that the unconstrained ACI response is not robust. However, the Low-SSA group shows increased cloud fraction and precipitation over the Sahel, together with a more negative Sahel ERF_{aci}^{SW}, consistent with enhanced SW reflection by increased cloudiness. The response also projects onto the tropical North Atlantic as part of a Sahel–TNA cloud-radiative dipole. This suggests that the ACI response is not independent of the dust $\mathbf{ERF}_{\mathbf{ari}}^{\mathbf{SW}}$, but is partly organized by the SSA-dependent circulation adjustment.

The observational constraint is propagated to the cloud response in two steps. The AERONET-based SSA constraint first constrains Sahara-mean ERF_{ari}^{SW}, and the resulting constrained $\mathbf{ERF}_{\mathbf{ari}}^{\mathbf{SW}}$ distribution is then passed through the inter-model relationship between Sahara ERF_{ari}^{SW} and Sahel ERF_{aci}^{SW}. This physical and dynamical pathway from SSA_{obs} to ERF_{ari}^{SW}, and to ERF_{aci}^{SW} reduces the spread of Sahel ERF_{aci}^{SW}. The standard deviation decreases from 2.33 to 1.87 W m^{-2}, corresponding to a reduction of about 20 %, or roughly one third of the variance. However, the constrained range still spans zero, so the sign of the Sahel SW cloud-radiative response remains unresolved.

The variance decomposition shows why this uncertainty remains. Only a small fraction of the posterior variance is associated with observational SSA uncertainty. Most of the remaining variance comes from the residual scatter in the SSA-to-ERF_{ari}^{SW} relationship and in the ERF_{ari}^{SW}-to-ERF_{aci}^{SW} relationship. This indicates that improving the observational precision of SSA alone would not fully resolve the problem. Further progress requires constraints on dust particle size, vertical distribution, and other extensive dust properties that affect $\mathbf{ERF}_{\mathbf{ari}}^{\mathbf{SW}}$, as well as better representation of circulation-cloud coupling and cloud-radiative processes that control the downstream ACI response.

Because the piClim experiments prescribe SSTs, these results should be interpreted as rapid atmospheric adjustments to dust forcing rather than as fully coupled monsoon responses. The central conclusion is therefore not that SSA uniquely determines the Sahel cloud response. Rather, an observable dust optical property organizes a substantial part of the pathway from Saharan $\mathbf{ERF}_{\mathbf{ari}}^{\mathbf{SW}}$ to monsoon circulation and downstream cloud-radiative adjustment. The SSA constraint reduces uncertainty in both local $\mathbf{ERF}_{\mathbf{ari}}^{\mathbf{SW}}$ and remote Sahel cloud response, but it does not eliminate sign uncertainty. This result highlights the value of intensive optical constraints for regional aerosol-climate studies, while also showing where additional model and observational constraints are needed to reduce uncertainty in dust-driven monsoon and cloud responses.

https://doi.org/10.5194/egusphere-2026-6804
Preprint. Discussion started: 12 November 2026
© Author(s) 2026. CC BY 4.0 License.

Appendix A: APRP term grouping used in this study

We use the Approximate Partial Radiative Perturbation (APRP) method to decompose the SW TOA radiative response between piClim-control and piClim-2xdust into surface-albedo, non-cloud atmospheric, and cloud-mediated components. The full APRP formulation is given by Taylor et al. (2007) and Zelinka et al. (2014). Here we describe only the term grouping and implementation used in this study.

For each model, APRP is applied to monthly radiative fluxes from piClim-control and piClim-2xdust. The perturbation is defined as piClim-2xdust minus piClim-control. Each APRP-diagnosed planetary-albedo contribution is converted to a TOA SW flux anomaly as

$$\Delta F_x = -\mathrm{SW}^{\downarrow}\,\Delta A_x, \qquad \text{(A1)}$$

where $\mathrm{SW}^{\downarrow}$ is the incoming SW radiation at the TOA, and ΔA_x is the APRP-diagnosed contribution to planetary albedo change from term x. Positive ΔF_x therefore denotes an increase in net downward SW radiation at the TOA.

Following Zelinka et al. (2014), the APRP decomposition yields nine SW terms. In this study, t_1 and t_4 denote the clear-sky and overcast surface-albedo contributions. Terms t_2 and t_3 denote the clear-sky non-cloud atmospheric scattering and absorption contributions. Terms t_5 and t_6 denote the overcast non-cloud atmospheric scattering and absorption contributions. Term t_7 denotes the cloud-fraction contribution, and t_8 and t_9 denote cloud scattering and cloud absorption contributions.

The scaling uses the downwelling TOA SW flux rather than the net SW flux, following Zelinka et al. (2014). Because prescribed insolation is identical in piClim-control and piClim-2xdust, $\mathrm{SW}^{\downarrow}$ is the same in the two experiments.

We define $\mathbf{ERF}^{\mathbf{SW}}_{\mathbf{ari}}$ as the sum of the non-cloud atmospheric scattering and absorption terms,

$$\mathrm{ERF}^{\mathrm{SW}}_{\mathrm{ari}} = t_2 + t_3 + t_5 + t_6. \qquad \text{(A2)}$$

Here, $\mathrm{ERF}^{\mathrm{SW}}_{\mathrm{ari}}$ represents the non-cloud atmospheric scattering and absorption response. For the scattering–absorption decomposition used in Sect. 3.2, we further separate this term into

$$\mathrm{ERF}^{\mathrm{SW}}_{\mathrm{ari,scat}} = t_2 + t_5, \text{ and} \qquad \text{(A3)}$$

$$\mathrm{ERF}^{\mathrm{SW}}_{\mathrm{ari,abs}} = t_3 + t_6. \qquad \text{(A4)}$$

$\mathrm{ERF}^{\mathrm{SW}}_{\mathrm{aci}}$ is defined as the sum of the cloud-mediated terms,

$$\mathrm{ERF}^{\mathrm{SW}}_{\mathrm{aci}} = t_7 + t_8 + t_9. \qquad \text{(A5)}$$

https://doi.org/10.5194/egusphere-2026-6804
Preprint. Discussion started: 12 November 2026
© Author(s) 2026. CC BY 4.0 License.

Here, $\mathrm{ERF}_{\mathrm{aci}}^{\mathrm{SW}}$ represents the cloud-mediated SW response. It should therefore be interpreted as a cloud-radiative adjustment associated with the dust perturbation, not necessarily as a purely microphysical dust-cloud interaction.

The SW surface-albedo contribution is defined as

$$\mathrm{ERF}_{\mathrm{alb}}^{\mathrm{SW}} = t_1 + t_4. \qquad \text{(A6)}$$

The LW terms are diagnosed separately because APRP is a SW albedo decomposition. We define $\mathrm{ERF}_{\mathrm{aci}}^{\mathrm{LW}}$ as the change in LW cloud radiative effect,

$$\mathrm{ERF}_{\mathrm{aci}}^{\mathrm{LW}} = \Delta\left(\mathrm{LW}_{\mathrm{clr}}^{\uparrow} - \mathrm{LW}^{\uparrow}\right), \qquad \text{(A7)}$$

and $\mathbf{ERF}_{\mathbf{ari}}^{\mathbf{LW}}$ as the clear-sky residual,

$$\mathrm{ERF}_{\mathrm{ari}}^{\mathrm{LW}} = -\Delta\,\mathrm{LW}_{\mathrm{clr}}^{\uparrow}. \qquad \text{(A8)}$$

Their sum gives the total LW TOA response,

$$\mathrm{ERF}_{\mathrm{ari}}^{\mathrm{LW}} + \mathrm{ERF}_{\mathrm{aci}}^{\mathrm{LW}} = -\Delta\,\mathrm{LW}^{\uparrow}. \qquad \text{(A9)}$$

All APRP terms are computed from monthly fields on each model native grid, averaged over the 30-year climatology, and then regridded to the common 1° × 1° analysis grid. A minimum cloud-fraction threshold of 0.02 is applied only to the overcast and cloud-related terms, t_4–t_9, to avoid unstable overcast reconstruction when cloud fraction is very small. The clear-sky aerosol terms t_2 and t_3, which contain the clearest Saharan dust absorption signal, are unaffected by this threshold.

This grouping is used to identify whether the inter-model spread in Saharan $\mathrm{ERF}_{\mathrm{ari}}^{\mathrm{SW}}$ arises mainly from dust scattering or dust absorption, while retaining a consistent decomposition for all models using standard archived radiative fluxes.

Appendix B: Sensitivity of Saharan column SSA to the low-extinction threshold

Grid-cell SSA can become unstable where total aerosol optical depth is very small, because the ratio $\tau_{\mathrm{abs,aer}}^{550} / \tau_{\mathrm{ext,aer}}^{550}$ is then sensitive to small numerical differences. We therefore tested whether the Saharan-mean SSA depends on the low-extinction threshold used when obtaining grid-cell SSA. We repeated the calculation using $\tau_{\mathrm{ext,aer}}^{550}$ thresholds from 0.001 to 0.01. The Saharan-mean SSA changes negligibly across this range, and the model ordering remains unchanged. This weak sensitivity reflects the fact that the Saharan land mask is dominated by optically thick dust-laden grid cells. The threshold therefore has

https://doi.org/10.5194/egusphere-2026-6804
Preprint. Discussion started: 12 November 2026
© Author(s) 2026. CC BY 4.0 License.

little influence on the regional SSA used in the main analysis.

Appendix C: AERONET inversion products and Saharan SSA estimate

We estimate Saharan dust SSA from AERONET Version 3 Level 2.0 inversion products at five stations within or near the Saharan dust domain, Tamanrasset, El Farafra, Ouarzazate, Bordj Badji Mokhtar, and Bodélé. AERONET inversion products retrieve columnar aerosol optical properties from Sun and sky radiance measurements, and Level 2.0 products are quality-assured and cloud-screened. Because reliable SSA retrievals require sufficiently high aerosol loading, the selected observations preferentially sample dust-dominated conditions over these Saharan and near-Saharan stations.

AERONET reports SSA at 440, 675, 870, and 1020 nm. We interpolate the spectral SSA to 550 nm using a cubic spline and average the five station values. The resulting Saharan dust SSA is 0.9543, with an inter-station standard deviation of 0.0060, which we use as a conservative measure of regional representativeness uncertainty. As an independent check, North African dust measurements from Di Biagio et al. (2019) give a source-mean SSA of about 0.957 at wavelengths bracketing 550 nm, close to the AERONET-based estimate. The Bodélé soil sample from Di Biagio et al. (2019) is not used in the constraint because its diatomite-rich composition gives an anomalously high SSA that is not representative of typical North African dust.

Appendix D: Emergent-constraint uncertainty propagation

The emergent constraint is first applied to the relationship between Saharan column SSA and Saharan $\mathbf{ERF}_{\mathbf{ari}}^{\mathbf{SW}}$ across the eight-model ensemble. For model i, we define X_i as Saharan column SSA, and Y_i as Sahara-mean $\mathrm{ERF}_{\mathrm{ari}}^{\mathrm{SW}}$. We fit an ordinary least-squares (OLS) regression,

$$Y_i = \beta_0 + \beta_1 X_i + \epsilon_i, \qquad \text{(D1)}$$

where β_0 and β_1 are the intercept and slope, and ϵ_i is the residual.

Predictive uncertainty is estimated using the standard OLS prediction error, including both regression residual variance and uncertainty in the fitted mean response. The 95 % prediction interval is then calculated using the Student-t quantile with $n - 2$ degrees of freedom.

To propagate the observational SSA constraint, we draw 4×10^5 samples from

$$X_{\mathrm{obs}} \sim \mathcal{N}\left(0.9543, 0.0060^2\right).$$

https://doi.org/10.5194/egusphere-2026-6804
Preprint. Discussion started: 12 November 2026
© Author(s) 2026. CC BY 4.0 License.

For each sampled SSA value, we evaluate the regression prediction and add a Gaussian perturbation with the corresponding prediction uncertainty. The resulting distribution combines observational SSA uncertainty and regression predictive uncertainty. We report its mean and 2.5th–97.5th percentile range as the SSA-constrained estimate of Sahara-mean $\mathrm{ERF}_{\mathrm{ari}}^{\mathrm{SW}}$.

Code and data availability

All CMIP6 model output used in this study was obtained from the Earth System Grid Federation (https://esgf-node.llnl.gov/projects/cmip6/, last access: 2 July 2026). The AerChemMIP piClim-control and piClim-2xdust simulations use the r1i1p1f1 variant for EC-Earth3-AerChem, MPI-ESM-1-2-HAM, NorESM2-LM, IPSL-CM6A-LR-INCA, GFDL-ESM4, and MIROC6, the r1i1p1f2 variant for CNRM-ESM2-1, and the r1i1p1f4 variant for UKESM1-0-LL. The historical simulations use the same variants, except for UKESM1-0-LL, for which the standard r1i1p1f2 variant is used because the AerChemMIP forcing index is not available for that experiment.

AERONET Version 3 Level 2.0 inversion products are available from https://aeronet.gsfc.nasa.gov (last access: 14 May 2026). GPCP Precipitation Level 3 Monthly 0.5° V3.3 (GPCPMON) data are available from the NASA Goddard Earth Sciences Data and Information Services Center (https://doi.org/10.5067/MEASURES/GPCP/DATA306, last access: 22 June 2026), and CHIRPS version 2.0 from https://www.chc.ucsb.edu/data/chirps (last access: 23 June 2026). MODIS Aqua Level 3 monthly aerosol products (MYD08_M3) are available from https://ladsweb.modaps.eosdis.nasa.gov (last access: 27 February 2026), and the MISR Level 3 Component Global Aerosol product (MIL3DAEN version 004) from the NASA Langley Atmospheric Science Data Center (https://asdc.larc.nasa.gov/project/MISR, last access: 25 June 2026).

The analysis code used in this study, including the APRP processing scripts and the scripts used to generate all figures, is available at https://doi.org/10.5281/zenodo.23907868 (Kang, 2026).

Author contributions

WK conceptualized the study, performed the analysis, produced the figures, and wrote the original draft. MIL supervised the study and provided comments that improved the manuscript. KMK contributed to the discussion of the results and provided comments on the manuscript. KOB, PHC, and HL acquired the funding and administered the project. All authors reviewed and approved the final manuscript.

https://doi.org/10.5194/egusphere-2026-6804
Preprint. Discussion started: 12 November 2026
© Author(s) 2026. CC BY 4.0 License.

Competing interests

The authors declare that they have no conflict of interest.

Acknowledgements

We acknowledge the World Climate Research Programme, which, through its Working Group on Coupled Modelling, coordinated and promoted CMIP6. We thank the climate modelling groups for producing and making available their model output, and the Earth System Grid Federation for archiving the data and providing access. We thank the principal investigators and their staff for establishing and maintaining the five AERONET sites used in this study.

Financial support

This research has been supported by the Korea Meteorological Administration Research and Development Program “Development and Assessment of Climate Change Scenario” (grant no. KMA2018-00321).

References

Adebiyi, A. A., Huang, Y., Samset, B. H., and Kok, J. F.: Observations suggest that North African dust absorbs less solar radiation than models estimate, Commun. Earth Environ., 4, 168, https://doi.org/10.1038/s43247-023-00825-2, 2023.

Bauer, S. E., Mishchenko, M. I., Lacis, A. A., Zhang, S., Perlwitz, J., and Metzger, S. M.: Do sulfate and nitrate coatings on mineral dust have important effects on radiative properties and climate modeling?, J. Geophys. Res., 112, D06307, https://doi.org/10.1029/2005JD006977, 2007.

Claquin, T., Schulz, M., Balkanski, Y., and Boucher, O.: Uncertainties in assessing radiative forcing by mineral dust, Tellus B, 50, 491–505, https://doi.org/10.1034/j.1600-0889.1998.t01-2-00007.x, 1998.

Collins, W. J., Lamarque, J.-F., Schulz, M., Boucher, O., Eyring, V., Hegglin, M. I., Maycock, A., Myhre, G., Prather, M., Shindell, D., and Smith, S. J.: AerChemMIP: quantifying the effects of chemistry and aerosols in CMIP6, Geosci. Model Dev., 10, 585–607, https://doi.org/10.5194/gmd-10-585-2017, 2017.

Di Biagio, C., Formenti, P., Balkanski, Y., Caponi, L., Cazaunau, M., Pangui, E., Journet, E., Nowak, S.,

https://doi.org/10.5194/egusphere-2026-6804
Preprint. Discussion started: 12 November 2026
© Author(s) 2026. CC BY 4.0 License.

Andreae, M. O., Kandler, K., Saeed, T., Piketh, S., Seibert, D., Williams, E., and Doussin, J.-F.: Complex refractive indices and single-scattering albedo of global dust aerosols in the shortwave spectrum and relationship to size and iron content, Atmos. Chem. Phys., 19, 15503–15531, https://doi.org/10.5194/acp-19-15503-2019, 2019.

Dubovik, O. and King, M. D.: A flexible inversion algorithm for retrieval of aerosol optical properties from Sun and sky radiance measurements, J. Geophys. Res., 105, 20673–20696, https://doi.org/10.1029/2000JD900282, 2000.

Dufresne, J.-L., Gautier, C., Ricchiazzi, P., and Fouquart, Y.: Longwave scattering effects of mineral aerosols, J. Atmos. Sci., 59, 1959–1966, https://doi.org/10.1175/1520-0469(2002)059<1959:LSEOMA>2.0.CO;2, 2002.

Froyd, K. D., Yu, P., Schill, G. P., Brock, C. A., Kupc, A., Williamson, C. J., Jensen, E. J., Ray, E., Rosenlof, K. H., Bian, H., Darmenov, A. S., Colarco, P. R., Diskin, G. S., Bui, T., and Murphy, D. M.: Dominant role of mineral dust in cirrus cloud formation revealed by global-scale measurements, Nat. Geosci., 15, 177–183, https://doi.org/10.1038/s41561-022-00901-w, 2022.

Giles, D. M., Sinyuk, A., Sorokin, M. G., Schafer, J. S., Smirnov, A., Slutsker, I., Eck, T. F., Holben, B. N., Lewis, J. R., Campbell, J. R., Welton, E. J., Korkin, S. V., and Lyapustin, A. I.: Advancements in the Aerosol Robotic Network (AERONET) Version 3 database – automated near-real-time quality control algorithm with improved cloud screening for Sun photometer aerosol optical depth (AOD) measurements, Atmos. Meas. Tech., 12, 169–209, https://doi.org/10.5194/amt-12-169-2019, 2019.

Gliß, J., Mortier, A., Schulz, M., Andrews, E., Balkanski, Y., Bauer, S. E., Benedictow, A. M. K., Bian, H., Checa-Garcia, R., Chin, M., Ginoux, P., Griesfeller, J. J., Heckel, A., Kipling, Z., Kirkevåg, A., Kokkola, H., Laj, P., Le Sager, P., Lund, M. T., Lund Myhre, C., Matsui, H., Myhre, G., Neubauer, D., van Noije, T., North, P., Olivié, D. J. L., Rémy, S., Sogacheva, L., Takemura, T., Tsigaridis, K., and Tsyro, S. G.: AeroCom phase III multi-model evaluation of the aerosol life cycle and optical properties using ground- and space-based remote sensing as well as surface in situ observations, Atmos. Chem. Phys., 21, 87–128, https://doi.org/10.5194/acp-21-87-2021, 2021.

Haugvaldstad, O. W., Olivié, D., Storelvmo, T., and Schulz, M.: Dust radiative forcing in CMIP6 Earth System models: insights from the AerChemMIP piClim-2xdust experiment, Atmos. Chem. Phys., 25, 13199–13219, https://doi.org/10.5194/acp-25-13199-2025, 2025.

Hess, M., Koepke, P., and Schult, I.: Optical Properties of Aerosols and Clouds: The software package OPAC, Bull. Am. Meteorol. Soc., 79, 831–844, https://doi.org/10.1175/1520-

https://doi.org/10.5194/egusphere-2026-6804
Preprint. Discussion started: 12 November 2026
© Author(s) 2026. CC BY 4.0 License.

0477(1998)079<0831:OPOAAC>2.0.CO;2, 1998.

Hooper, J. and Marx, S.: A global doubling of dust emissions during the Anthropocene?, Glob. Planet. Change, 169, 70–91, https://doi.org/10.1016/j.gloplacha.2018.07.003, 2018.

Huneeus, N., Schulz, M., Balkanski, Y., Griesfeller, J., Prospero, J., Kinne, S., Bauer, S., Boucher, O., Chin, M., Dentener, F., Diehl, T., Easter, R., Fillmore, D., Ghan, S., Ginoux, P., Grini, A., Horowitz, L., Koch, D., Krol, M. C., Landing, W., Liu, X., Mahowald, N., Miller, R., Morcrette, J.-J., Myhre, G., Penner, J., Perlwitz, J., Stier, P., Takemura, T., and Zender, C. S.: Global dust model intercomparison in AeroCom phase I, Atmos. Chem. Phys., 11, 7781–7816, https://doi.org/10.5194/acp-11-7781-2011, 2011.

Juckes, M., Taylor, K. E., Durack, P. J., Lawrence, B., Mizielinski, M. S., Pamment, A., Peterschmitt, J.-Y., Rixen, M., and Sénési, S.: The CMIP6 Data Request (DREQ, version 01.00.31), Geosci. Model Dev., 13, 201–224, https://doi.org/10.5194/gmd-13-201-2020, 2020.

Kang, W.: Analysis code for “Single-scattering albedo drives Saharan dust forcing uncertainty and the simulated West African monsoon response in CMIP6 models”, Zenodo [code], https://doi.org/10.5281/zenodo.23907868, 2026.

Karydis, V. A., Tsimpidi, A. P., Bacer, S., Pozzer, A., Nenes, A., and Lelieveld, J.: Global impact of mineral dust on cloud droplet number concentration, Atmos. Chem. Phys., 17, 5601–5621, https://doi.org/10.5194/acp-17-5601-2017, 2017.

Kok, J. F., Ridley, D. A., Zhou, Q., Miller, R. L., Zhao, C., Heald, C. L., Ward, D. S., Albani, S., and Haustein, K.: Smaller desert dust cooling effect estimated from analysis of dust size and abundance, Nat. Geosci., 10, 274–278, https://doi.org/10.1038/ngeo2912, 2017.

Kok, J. F., Adebiyi, A. A., Albani, S., Balkanski, Y., Checa-Garcia, R., Chin, M., Colarco, P. R., Hamilton, D. S., Huang, Y., Ito, A., Klose, M., Li, L., Mahowald, N. M., Miller, R. L., Obiso, V., Pérez García-Pando, C., Rocha-Lima, A., and Wan, J. S.: Contribution of the world's main dust source regions to the global cycle of desert dust, Atmos. Chem. Phys., 21, 8169–8193, https://doi.org/10.5194/acp-21-8169-2021, 2021.

Kok, J. F., Storelvmo, T., Karydis, V. A., Adebiyi, A. A., Mahowald, N. M., Evan, A. T., He, C., and Leung, D. M.: Mineral dust aerosol impacts on global climate and climate change, Nat. Rev. Earth Environ., 4, 71–86, https://doi.org/10.1038/s43017-022-00379-5, 2023.

Lavaysse, C., Flamant, C., Janicot, S., Parker, D. J., Lafore, J.-P., Sultan, B., and Pelon, J.: Seasonal evolution of the West African heat low: a climatological perspective, Clim. Dynam., 33, 313–330,

https://doi.org/10.5194/egusphere-2026-6804
Preprint. Discussion started: 12 November 2026
© Author(s) 2026. CC BY 4.0 License.

https://doi.org/10.1007/s00382-009-0553-4, 2009.

Li, L., Mahowald, N. M., Gonçalves Ageitos, M., Obiso, V., Miller, R. L., Pérez García-Pando, C., Di Biagio, C., Formenti, P., Brodrick, P. G., Clark, R. N., Green, R. O., Kokaly, R., Swayze, G., and Thompson, D. R.: Improved constraints on hematite refractive index for estimating climatic effects of dust aerosols, Commun. Earth Environ., 5, 295, https://doi.org/10.1038/s43247-024-01441-4, 2024.

Mallet, M., Nabat, P., Johnson, B., Michou, M., Haywood, J. M., Chen, C., and Dubovik, O.: Climate models generally underrepresent the warming by Central Africa biomass-burning aerosols over the Southeast Atlantic, Sci. Adv., 7, eabg9998, https://doi.org/10.1126/sciadv.abg9998, 2021.

Miller, R. L., Tegen, I., and Perlwitz, J.: Surface radiative forcing by soil dust aerosols and the hydrologic cycle, J. Geophys. Res., 109, D04203, https://doi.org/10.1029/2003JD004085, 2004.

Mulitza, S., Heslop, D., Pittauerová, D., Fischer, H. W., Meyer, I., Stuut, J.-B., Zabel, M., Mollenhauer, G., Collins, J. A., Kuhnert, H., and Schulz, M.: Increase in African dust flux at the onset of commercial agriculture in the Sahel region, Nature, 466, 226–228, https://doi.org/10.1038/nature09213, 2010.

Myhre, G. and Stordal, F.: Global sensitivity experiments of the radiative forcing due to mineral aerosols, J. Geophys. Res., 106, 18193–18204, https://doi.org/10.1029/2000JD900536, 2001.

Obiso, V., Gonçalves Ageitos, M., Pérez García-Pando, C., Perlwitz, J. P., Schuster, G. L., Bauer, S. E., Di Biagio, C., Formenti, P., Tsigaridis, K., and Miller, R. L.: Observationally constrained regional variations of shortwave absorption by iron oxides emphasize the cooling effect of dust, Atmos. Chem. Phys., 24, 5337–5367, https://doi.org/10.5194/acp-24-5337-2024, 2024.

Pan, B., Wang, Y., Hu, J., Lin, Y., Hsieh, J.-S., Logan, T., Feng, X., Jiang, J. H., Yung, Y. L., and Zhang, R.: Impacts of Saharan dust on Atlantic regional climate and implications for tropical cyclones, J. Climate, 31, 7621–7644, https://doi.org/10.1175/JCLI-D-16-0776.1, 2018.

Shell, K. M. and Somerville, R. C. J.: Direct radiative effect of mineral dust and volcanic aerosols in a simple aerosol climate model, J. Geophys. Res., 112, D03205, https://doi.org/10.1029/2006JD007197, 2007.

Shi, T., Cui, J., Chen, Y., Zhou, Y., Pu, W., Xu, X., Chen, Q., Zhang, X., and Wang, X.: Enhanced light absorption and reduced snow albedo due to internally mixed mineral dust in grains of snow, Atmos. Chem. Phys., 21, 6035–6051, https://doi.org/10.5194/acp-21-6035-2021, 2021.

https://doi.org/10.5194/egusphere-2026-6804
Preprint. Discussion started: 12 November 2026
© Author(s) 2026. CC BY 4.0 License.



Solmon, F., Mallet, M., Elguindi, N., Giorgi, F., Zakey, A., and Konaré, A.: Dust aerosol impact on regional precipitation over western Africa, mechanisms and sensitivity to absorption properties, Geophys. Res. Lett., 35, L24705, https://doi.org/10.1029/2008GL035900, 2008.

Storelvmo, T.: Aerosol effects on climate via mixed-phase and ice clouds, Annu. Rev. Earth Planet. Sci., 45, 199–222, https://doi.org/10.1146/annurev-earth-060115-012240, 2017.

Strong, J. D. O., Vecchi, G. A., and Ginoux, P.: The response of the tropical Atlantic and West African climate to Saharan dust in a fully coupled GCM, J. Climate, 28, 7071–7092, https://doi.org/10.1175/JCLI-D-14-00797.1, 2015.

Taylor, K. E., Crucifix, M., Braconnot, P., Hewitt, C. D., Doutriaux, C., Broccoli, A. J., Mitchell, J. F. B., and Webb, M. J.: Estimating shortwave radiative forcing and response in climate models, J. Climate, 20, 2530–2543, https://doi.org/10.1175/JCLI4143.1, 2007.

Thornhill, G., Collins, W., Olivié, D., Skeie, R. B., Archibald, A., Bauer, S., Checa-Garcia, R., Fiedler, S., Folberth, G., Gjermundsen, A., Horowitz, L., Lamarque, J.-F., Michou, M., Mulcahy, J., Nabat, P., Naik, V., O'Connor, F. M., Paulot, F., Schulz, M., Scott, C. E., Séférian, R., Smith, C., Takemura, T., Tilmes, S., Tsigaridis, K., and Weber, J.: Climate-driven chemistry and aerosol feedbacks in CMIP6 Earth system models, Atmos. Chem. Phys., 21, 1105–1126, https://doi.org/10.5194/acp-21-1105-2021, 2021.

Toolan, C. A., Amooli, J. A., Wilcox, L. J., Samset, B. H., Turner, A. G., and Westervelt, D. M.: Strong intermodel differences and biases in CMIP6 simulations of PM2.5, aerosol optical depth, and precipitation over Africa, Atmos. Chem. Phys., 25, 10523–10557, https://doi.org/10.5194/acp-25-10523-2025, 2025.

Wilcox, E. M., Lau, K. M., and Kim, K.-M.: A northward shift of the North Atlantic Ocean Intertropical Convergence Zone in response to summertime Saharan dust outbreaks, Geophys. Res. Lett., 37, L04804, https://doi.org/10.1029/2009GL041774, 2010.

Zelinka, M. D., Andrews, T., Forster, P. M., and Taylor, K. E.: Quantifying components of aerosol-cloud-radiation interactions in climate models, J. Geophys. Res. Atmos., 119, 7599–7615, https://doi.org/10.1002/2014JD021710, 2014.

Zhao, A., Ryder, C. L., and Wilcox, L. J.: How well do the CMIP6 models simulate dust aerosols?, Atmos. Chem. Phys., 22, 2095–2119, https://doi.org/10.5194/acp-22-2095-2022, 2022.

Zhao, A., Wilcox, L. J., and Ryder, C. L.: The key role of atmospheric absorption in the Asian summer monsoon response to dust emissions in CMIP6 models, Atmos. Chem. Phys., 24, 13385–13402,

https://doi.org/10.5194/egusphere-2026-6804
Preprint. Discussion started: 12 November 2026
© Author(s) 2026. CC BY 4.0 License.



926 https://doi.org/10.5194/acp-24-13385-2024, 2024.

927